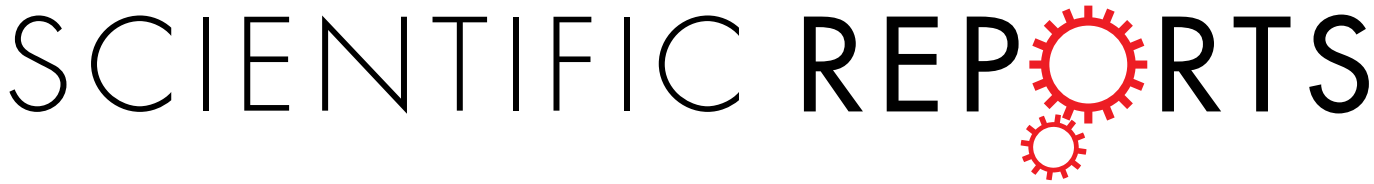

OPEN

Measurements of three-dimensional refractive index tomography and membrane deformability of live erythrocytes from *Pelophylax nigromaculatus*

Received: 26 October 2017
Accepted: 17 April 2018
Published online: 15 June 2018

Geon Kim[1,2], Moosung Lee[1,2], SeongYeon Youn[3], EuiTae Lee[3], Daeheon Kwon[3], Jonghun Shin[3], SangYun Lee[1,2], Youn Sil Lee[3] & YongKeun Park[1,2,4]

Unlike mammalian erythrocytes, amphibian erythrocytes have distinct morphological features including large cell sizes and the presence of nuclei. The sizes of the cytoplasm and nuclei of erythrocytes vary significantly over different species, their environments, or pathophysiology, which makes hematological studies important for investigating amphibian species. Here, we present a label-free three-dimensional optical quantification of individual amphibian erythrocytes from frogs *Pelophylax nigromaculatus (Rana nigromaculata)*. Using optical diffraction tomography, we measured three-dimensional refractive index (RI) tomograms of the cells, which clearly distinguished the cytoplasm and nuclei of the erythrocytes. From the measured RI tomograms, we extracted the relevant biochemical parameters of the cells, including hemoglobin contents and hemoglobin concentrations. Furthermore, we measured dynamic membrane fluctuations and investigated the mechanical properties of the cell membrane. From the statistical and correlative analysis of these retrieved parameters, we investigated interspecific differences between frogs and previously studied mammals.

The properties of erythrocytes are related to the cellular functions in the circulatory system. For example, the ability of erythrocytes to squeeze through capillary vessels is crucial in the transportation of oxygen to organs. A detailed understanding of amphibian erythrocytes can offer new aspects of the amphibian physiology. Furthermore, in the evolutionary point of view, hematological studies of amphibians play an important role in the study of their phylogenetic pathways following the vertebrate invasion of the land[1]. One of their critical traits of amphibians, compared to other vertebrates, is their unusually large erythrocytes, which may be associated with the adaptation for the transition from aquatic to terrestrial life. Because of their distinct morphologies, amphibian erythrocytes have been extensively investigated. Previous studies have suggested that the adaptive structures of the cells are dependent on both intrinsic factors including ages and species[2,3], and extrinsic factors including habitat conditions[4].

To quantitatively assess the various physiological properties of the cells, various experimental methods have been exploited. For example, bright-field microscopy has been used to quantify the size parameters of the cells in two-dimensions (2D), such as their aspect ratios[5]. However, this method has limitations when assessing the three-dimensional (3D) information of a cell. In addition, the method often relies on labeling methods such as fluorescent proteins or organic dyes, which may perturb the physiological conditions of the cells. Alternatively, a complete blood count was used for a high-throughput measurement of both morphological and biochemical parameters[6]. Electron microscopy was also implemented to visualize viral particles inside erythrocytes beyond

[1]Department of Physics, Korea Advanced Institute of Science and Technology (KAIST), Daejeon, 34141, South Korea. [2]KI for Health Science and Technology, KAIST, Daejeon, 34141, Republic of Korea. [3]Daejeon Science High School for the Gifted, Daejeon, 34142, Republic of Korea. [4]Tomocube, Inc., Daejeon, 34051, Republic of Korea. Geon Kim and Moosung Lee contributed equally to this work. Correspondence and requests for materials should be addressed to Y.P. (email: yk.park@kaist.ac.kr)

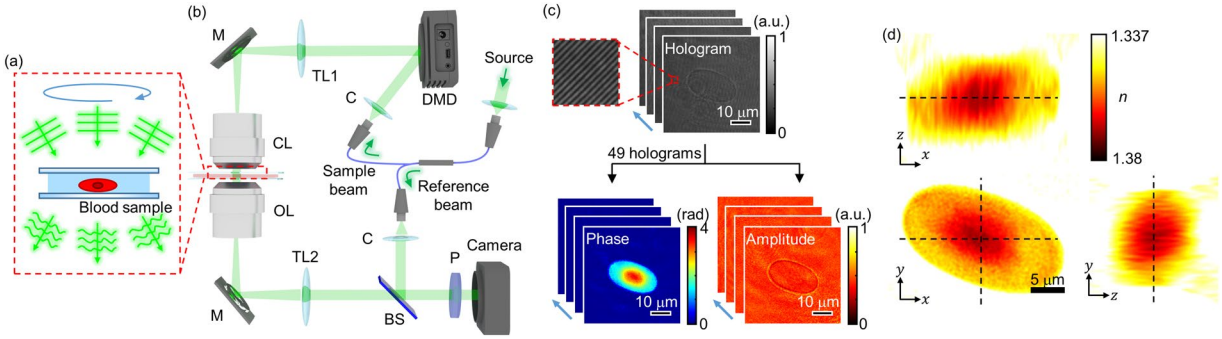

Figure 1. Principles of reconstructing 3D RI tomograms of frog erythrocytes using ODT. (**a**) Schematic diagram of image acquisition process in ODT. (**b**) Experimental setup. C: collimator; DMD: digital micromirror device; TL: tube lens; M: mirror, CL: condenser lens; OL: objective lens, BS: beam splitter; P: polarizer. (**c**) 49 measured off-axis holograms and retrieved phase and amplitude maps. (**d**) Cross sections of the reconstructed RI tomogram from the phase and amplitude maps in (**c**).

the optical diffraction limit[7]. However, these methods present challenges when studying the dynamics of live individual cells *in vitro*.

Recently, quantitative phase imaging (QPI) techniques have been developed as a label-free imaging method for the study of live cells and tissues[8,9]. QPI employs the principle of laser interferometric microscopy or digital holographic microscopy to measure the optical phase delay induced by a transparent specimen. Because the optical phase delay of a biological cell is linearly proportional to its thickness and relative refractive index (RI)[10], QPI provides a label-free, quantitative imaging capability with nanometer sensitivity. In particular, the morphology and biophysical properties of human erythrocytes and their pathophysiology have been extensively studied using this method[11–15].

In order to reconstruct 3D tomograms of unlabeled transparent cells, considerable advances have been made in tomographic QPI techniques[16–26]. Among them, optical diffraction tomography (ODT) or holotomography enables to reconstruct the 3D RI tomogram of a sample from multiple 2D QPI images with various illumination angles[20,27–29]. ODT has shown potential for precisely assessing the 3D morphological properties of mammalian blood cells at the individual cell level[30–34], and their related pathophysiologies, such as malaria or babesia infection[20,35–38]. Still, however, the extended capability of ODT for studying unlabeled cells from other species has not been thoroughly examined. One particular example is the amphibian erythrocyte, whose morphological and chemical properties of the nuclei and the cytoplasm have not been investigated using 3D QPI.

Here, we present 3D optical tomographic measurements of individual erythrocytes from frogs *Pelophylax nigromaculatus* (*Rana nigromaculata*). Using ODT, 3D RI tomograms of erythrocytes were measured at the individual cell level, which clearly visualized the 3D structures of the cytoplasm and nuclei, and provided morphological information such as cell volume and surface area, nucleus volume, surface area, and sphericity index. Exploiting the measured RI values, biochemical properties of the cells including hemoglobin (Hb) concentrations and contents were also retrieved. Furthermore, dynamic membrane fluctuations of individual live cells were measured, providing data on the biomechanical properties of the cell membranes. From the measured cellular parameters, we were able to compare the interspecific differences of erythrocytes from amphibians and formerly investigated mammals. Also, we examined the correlative relations between the retrieved parameters, which suggested the general characteristics of erythrocytes from different species.

Results and Discussions

3D RI tomograms of frog erythrocytes. The principle of ODT is illustrated in Fig. 1a. Similar to X-ray computed tomography (CT), ODT reconstructs the 3D tomogram of a sample from multiple 2D images of the sample obtained with various illumination angles[28]. While CT measures X-ray absorptivity in 3D, ODT measures RI tomography containing information about both the sample-induced light absorption and refraction.

In order to measure the 3D RI tomograms of frog erythrocytes, we utilized a commercial ODT setup[39,40] (HT-1S and HT-2S, Tomocube Inc.) [Fig. 1b]. The ODT setup is based on an off-axis Mach-Zehnder interferometer equipped with a digital micromirror device (DMD). A 2×2 single-mode fiber coupler splits a coherent, monochromatic laser (wavelength, $\lambda = 532$ nm) into a sample and a reference arm, respectively. To control the illumination angle of the beam impinging onto a sample, a DMD is utilized to diffract light into various angles[41,42]. The light scattered by the sample is then transmitted through an objective lens ($60\times$, numerical aperture $= 0.8$) and a tube lens ($f = 175$ mm). The sample beam is combined with the reference beam by a beam splitter and filtered by a linear polarizer. The resultant spatially modulated hologram is recorded by an image sensor. The image sensor is synchronized with the DMD to record 49 holograms of the sample illuminated with different angles (Fig. 1c). Using a phase retrieval algorithm[43,44], the amplitude and phase images are retrieved from the measured holograms. Based on the Fourier diffraction theorem with Rytov approximation[45], the 3D RI tomogram of the sample is reconstructed from the retrieved amplitude and phase images (Fig. 1d). The lateral and axial optical resolutions of the ODT system were 166 nm and 1 μm respectively, according to the Lauer criterion[46]. For 3D fluorescence imaging, multiple 2D epifluorescence images were captured at various axial locations, from which a 3D stacked fluorescence image is reconstructed after applying a deconvolution algorithm[40].

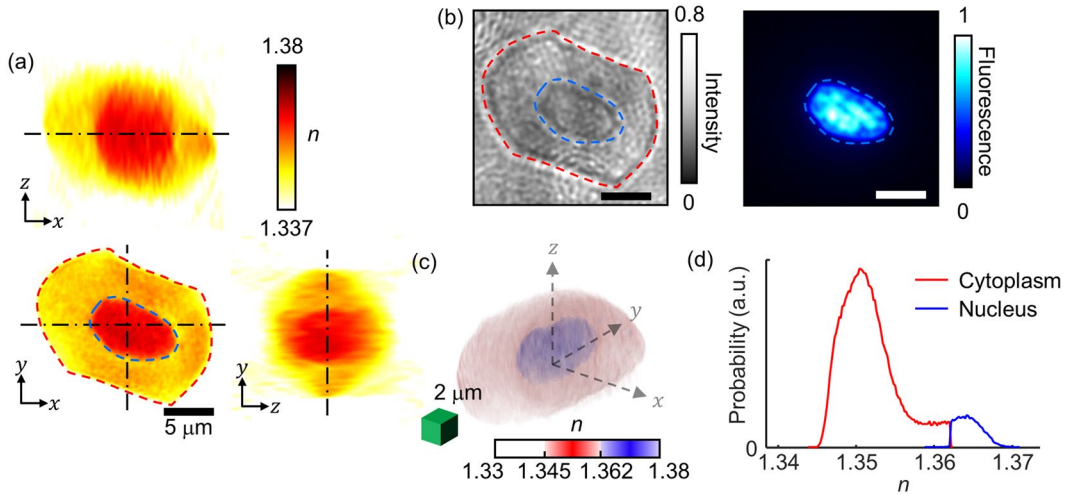

Figure 2. Structural analyses of frog erythrocytes using 3D RI maps. (**a**) Cross sections of the RI map of a frog erythrocyte. The red- and blue-dashed regions correspond to the cytoplasm and nucleus, respectively. (**b**) Bright-field image and DAPI fluorescence image for cross-validation of the cytoplasm and nucleus. (**c**) 3D-rendered isosurface image of the RI tomogram. (**d**) RI histograms for the cytoplasm and nucleus in (**c**).

Detailed information about the system and reconstruction algorithms can also be found elsewhere[20,28,47].

Anatomic structures of frog erythrocytes. Figure 2 presents the representative 3D RI structure of a frog erythrocyte. The cross-sections of the RI tomogram clearly show the ellipsoidal shape of a frog erythrocyte (Fig. 2a), which significantly differs from the biconcave shapes of mammalian erythrocytes. Also, the frog erythrocyte presents a central region whose RI values are higher than the outer region. The bright-field and 3D fluorescence images of the same sample stained with DAPI clearly indicate that this central area corresponds to a nucleus (Fig. 2b).

For quantitative analysis of the nucleus, the RI threshold between the cytoplasm and nucleus was determined to be 1.362, and was selected by comparing both the focal planes of the 3D RI tomograms and the 3D fluorescence images of the DAPI-stained cells. The cross-sectional images of the two images in different modalities showed a 93% correlation, verifying the RI threshold. Using the RI criterion, the cytoplasm and the nucleus of individual frog erythrocytes were segmented in 3D (Fig. 2c). The 3D isosurface image clearly visualizes the nucleus located in the middle of the cell. In addition, the averaged RI values of the nucleus and cytoplasm of the erythrocyte in Fig. 2a–c were measured and determined to be 1.365 ± 0.002 and 1.351 ± 0.004, respectively (Fig. 2d).

Morphological properties of frog erythrocytes. For a statistical analysis of the quantitative parameters of individual frog erythrocytes, we retrieved the volumes, surface areas, sphericity indices, Hb contents, and Hb concentrations of 128 erythrocytes from six frogs (Fig. 3). For interspecies analyses, we also compared each parameter of the frog erythrocytes with those of human and mouse erythrocytes, extracted from previous reports[37,48].

As is well known in 2D microscopy[3], frog erythrocytes exhibit distinct morphological parameters that are unlike human or mouse erythrocytes. The mean values of the cellular volumes of the frog erythrocytes were 1737.46 ± 299.32 fL, which was two orders of magnitude larger than that of human (90.5 ± 11.4 fL) and of mouse erythrocytes (45.6 ± 6.3 fL). Nucleus volumes of the amphibian cells were also measured to be 300.15 ± 167.07 fL, accounting for approximately 17% of the total erythrocyte volume. We believe that the broad range of the nucleus volumes is due to the cellular variance in RI distribution. The RI threshold which was established based on several erythrocytes may not be perfectly accurate for other erythrocytes. The mean values of the cellular surface areas of the frog erythrocytes were $892.35 \pm 119.07\,\mu m^2$, which was about six to nine times larger than human ($144.10 \pm 17.40\,\mu m^2$) and mouse erythrocytes ($102.00 \pm 13.00\,\mu m^2$). The nucleus surface areas were on average $267.88 \pm 106.39\,\mu m^2$, approximately 30% smaller than the cellular area.

To investigate size independent morphological properties of the erythrocytes, we measured their sphericity indices, the unitless parameters which quantify the shape resemblance to a sphere (Fig. 3c; see also *Methods*). The sphericity index is closer to one when the shape is closer to a sphere. The nuclei in the frog erythrocytes resembled ellipsoids; the average sphericity index of the nuclei was 0.80 ± 0.06. Like the nuclei, the membrane structures of the frog erythrocytes exhibited ellipsoidal shapes, whereas human and mouse erythrocytes exhibitied biconcave shapes. The average values of sphericity indexes were calculated to be 0.79 ± 0.08, 0.68 ± 0.06, and 0.63 ± 0.08 for the frog, human, and mouse erythrocytes, respectively.

Biochemical properties of frog erythrocytes. The biochemical properties of the cytoplasm, Hb concentrations, and contents were also obtained from the measured RI values (Fig. 3d; see also Methods). The result showed that the frog erythrocytes had significantly higher amounts of Hb contents than human and mouse erythrocytes. The retrieved Hb contents were 174.35 ± 33.93, 30.3 ± 4.8, and 16.40 ± 3.50 pg for frogs, humans, and

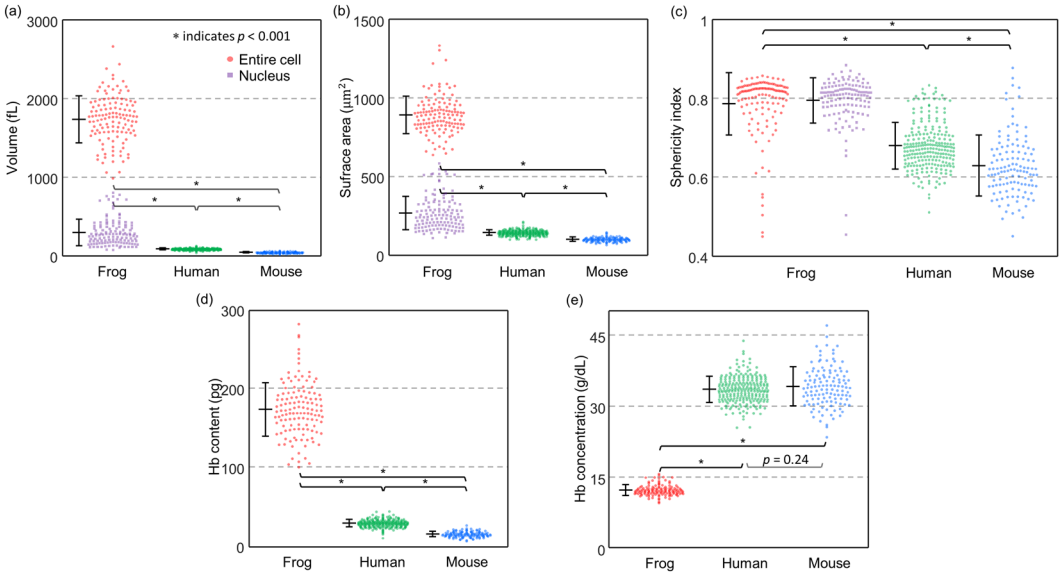

Figure 3. Statistical analyses of erythrocyte morphological and biochemical parameters for frogs, humans, and mice. (**a**–**c**) Distributions of morphological parameters including (**a**) volumes, (**b**) surface areas, and (**c**) sphericity indices. (**d,e**) Distributions of biochemical parameters including (**d**) Hb contents and (**e**) Hb concentrations. *indicates $p < 0.001$.

mice, respectively. The Hb contents of the frog erythrocytes measured by RI values were consistent with the previously estimated values for *Rana* frogs using the Sahli method[49]. The results showed that Hb concentrations in the frog groups were approximately three times lower than those of human and mouse groups (Fig. 3e). The measured Hb concentrations were 12.25 ± 1.12, 33.4 ± 2.8 and 34.0 ± 4.0 g/dL for frogs, humans, and mice, respectively. Note that these estimated low Hb concentrations of frog erythrocytes agree well with the previously reported values for mature *Rana* frogs[50].

Membrane deformability of frog erythrocytes. In order to investigate the membrane properties of the frog erythrocytes, we measured and quantified the dynamic fluctuations in the cell membrane (Fig. 4, see *Methods*). Membrane fluctuations of erythrocytes are strongly correlated with viscoelastic properties of the lipid membrane, spectrin network, and cytoplasmic viscosity, which can also be altered by diseases[11,12,14,48,51]. In previous studies, it has been shown that the dynamic fluctuations in mammalian erythrocyte membranes are driven by both the thermal and active metabolic energies[13,52,53], and related to their pathophysiology[12,35,48].

The dynamic membrane fluctuations in amphibian erythrocytes were quantitatively investigated. Figure 4a,b show the height (h) and the height change (Δh) in a frog erythrocyte, respectively. The relative height changes for 8 ms show the dynamic membrane fluctuations of the sample (Fig. 4b). We defined the spatially resolved membrane fluctuation profiles as the standard deviations of the temporal height distributions (σ_h), as in Fig. 4c. The membrane fluctuation map shows an inhomogeneous amplitude distribution over the cell membrane; the amplitude of the membrane fluctuation is slightly decreased near the nucleus. Considering cell structures, the decreased fluctuation near the nucleus can be explained by the presence of a stiff nucleus or cytoskeleton network anchoring the nucleus, or both[54]. For further investigation, correlative imaging with fluorescence microscopy would be helpful[28,55,56].

Then we compared the membrane fluctuations of frog, human, and mouse erythrocytes (Fig. 4d). The results showed that the membrane fluctuation of frog erythrocytes was approximately two times greater than those of human and mouse erythrocytes. The dynamic membrane fluctuations σ_h were 106.37 ± 14.72 nm, 55.10 ± 6.90 nm, and 57.10 ± 9.90 nm for frogs, humans, and mice, respectively. The interspecific differences in the membrane fluctuations may imply distinctions in mechanical properties of the erythrocytes between different species[57].

Correlative analysis of quantitative parameters of frog erythrocytes. We further examined the physiological characteristics of frog erythrocytes via correlative analyses of the retrieved parameters (Fig. 5). The scatterplot between the cell volumes and the Hb contents shows a positive linear correlation (Fig. 5a). The slopes obtained using least square fitting clearly indicate that for each species, Hb concentrations in individual cells do not vary significantly, regardless of the cell size. Although Hb concentrations in the human and mouse groups showed similar values (33.5 and 34.0 g/dL, respectively), the Hb concentration of the frog group showed a significantly lower value (10.0 g/dL). This result implies that homeostasis mechanisms for Hb concentration in amphibian erythrocytes differ from those of mammalian cells[58,59]. Note that the average ratio of Hb content to the cell volume is lower than the average Hb concentration for the frog erythrocytes, owing to the presence of the nuclei which occupy the volumes of the erythrocytes without containing Hb contents.

We also performed a correlative analysis of the Hb concentration and the membrane fluctuation (Fig. 5b). In the log-log scatterplot, the membrane fluctuations of the erythrocytes from the human and mouse groups

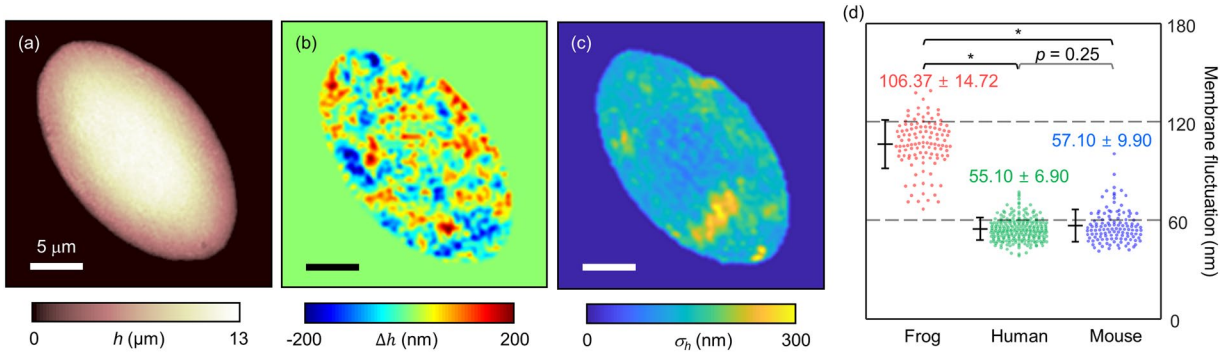

Figure 4. Measurement of temporal membrane fluctuation. (**a**) The thickness profile of a frog erythrocyte. (**b**) Instantaneous thickness shift of (**a**). (**c**) Membrane fluctuation map of (**a**). (**d**) Distributions of temporal membrane fluctuations of frogs, humans, and mice. *indicates $p < 0.001$.

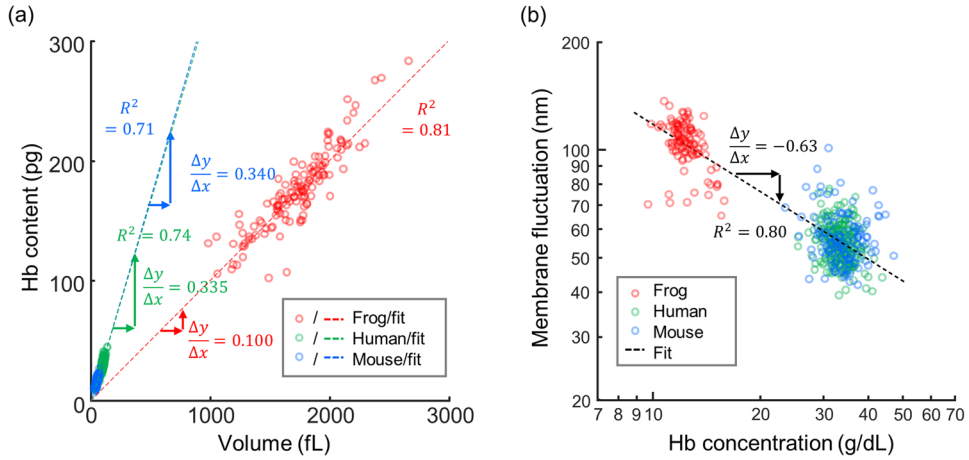

Figure 5. 2D Scatterplots of different erythrocyte parameters. (**a**) A scatterplot of volumes and Hb contents. (**b**) A log-log scatter plot of Hb concentrations and membrane fluctuations. R^2 indicates the R-squared value of the least square fitting.

had significantly different distributions from the distributions of the frog erythrocytes. The dynamic membrane fluctuations of the frog erythrocytes (106.37 ± 14.72 nm) were significantly higher than those of the human or mouse groups (55.10 ± 6.90 nm and 57.10 ± 9.90 nm). Significantly enhanced fluctuations would be expected for the frog erythrocytes based on a simple dimensional analysis because they are 20 times greater in volume and have 3 times lower cytoplasmic viscosity. However, these large fluctuations of the frog erythrocytes are not solely explained by these two effects. For example, the presence of the nucleus and anchoring cytoskeleton may affect this mechanical property of the frog erythrocytes. The molecular organizations of erythrocyte membrane structures differ between amphibians and mammalian species. Moreover, the αI spectrin gene[60], which is found in mammalian erythrocytes and causes enhanced deformability[61], is absent in frog erythrocytes, and this may also explain the low deformability of the frog erythrocytes. In addition, the mechanism of dynamic remodeling of membrane cortex structures mediated by ATP[13], which also plays a role in determining cellular deformability, may also differ in amphibian erythrocytes.

Conclusion

In summary, we present optical measurements of 3D RI tomograms and dynamic membrane fluctuations of amphibian erythrocytes of the frog *Pelophylax nigromaculatus*. From the measured RI tomograms, morphological (cell volume and surface area), biochemical (Hb concentration and content) and biomechanical (membrane deformability) properties were quantitatively retrieved. Furthermore, a correlative imaging approach was also employed to exploit both 3D RI tomography and 3D fluorescence imaging, and to enable the investigation of nuclei structures. Using a correlative analysis, these retrieved parameters were systematically investigated and also compared with mammalian erythrocytes from humans and mice.

Our correlative analysis using 3D QPI and fluorescence microscopy provides rich insight into the cellular structures and compositions depending on the species. For example, we have demonstrated that the nuclei of the frog erythrocytes have higher RI values than the cytoplasm, which is contrary to the recent reports that human leukemic cells have lower RI values in the nuclei[62,63]. This contrast may point to the hypothesis that the compositions of the subcellular compartments vary significantly over the species and their physiological states. Our recent

work indeed has verified the RI variations of nuclei and the cytoplasm over different eukaryotes[40]. Along with the advance of super-resolution imaging techniques[56], we anticipate that the extension of our presented methods will help to accurately quantify the RI distributions of subcellular compartments over various cell species.

Although the current study focused on measurements of frog erythrocytes, the approaches used here are general and can be readily applied to the study of the erythrocytes of other species. Furthermore, the QPI methods used for the study of mammalian erythrocytes can also be applied to further understand the mechanisms of amphibian blood cells, including the label-free visualization of parasites and host cells, the visualizations of white blood cells, and the effects of ATP to cell deformability. For example, the visualization of erythrocytes in microfluidic channels *in silico* or microcapillaries of frogs and tadpoles *in vivo*[64] would provide information valuable to unlocking the structures and dynamics of amphibian erythrocytes. In addition, this work could stimulate other disciplines including numerical simulations[65] and analytical modeling[66] of amphibian erythrocytes as well.

Materials and Methods

Sample preparation. Blood samples were prepared from six female frogs *Pelophylax nigromaculatus* (*Rana nigromaculata*) which had been bred for more than 2 years in a breeding farm where the temperature and humidity were maintained over 15 °C and 60% respectively. They were all fully grown, and the total length of their heads and torsos ranged from 8 to 9 cm, which is approximately the limit to which they grow. The blood was directly drawn from the heart of each frog using milliliter syringes (Sung Shim Medical, Republic of Korea) while the frogs were anesthetized with 99% ether, and then immediately stored in heparin-treated vacutainers (Becton Dickinson, Franklin Lakes, U.S.A.). The extracted blood was diluted in an isotonic amphibian phosphate-buffered saline solution, which was prepared by mixing 20% (w/w) deionized water and 80% (w/w) phosphate-buffered saline solution (Gibco®, New York, U.S.A.).

The diluted solution was separated into unstained groups and stained groups. The unstained groups were used to collect morphological, biochemical, and mechanical erythrocyte parameters with minimal perturbation. The other stained groups were prepared by fixation with 4% paraformaldehyde solution and stained with 3 μM DAPI solution, for the purpose of cross-correlating the locations of nuclei in the erythrocytes. For imaging purposes, a 50 μl drop of erythrocyte suspension was loaded between two coverslips spaced by a strip of double-sided Scotch tape. The loaded sample was then imaged at room temperature. All methods were performed in accordance with the relevant guidelines and regulations, which were approved by the institutional review board of KAIST (IRB project: KH2015-37).

Analyses of erythrocyte parameters. From the measured 3D RI tomograms of frog erythrocytes, various cellular parameters were quantitatively obtained and analyzed, including morphological (cell volume, nucleus volume, cell surface area, nucleus surface area, and sphericity index of cell shapes) and biochemical (Hb concentration and Hb content) parameters. The entire cell volume and the nucleus volume were directly retrieved using threshold values of RIs. Surface areas of the entire cells were also directly measured from the sample boundaries in 3D. To quantify the shape resemblance of a cell to a sphere, we calculated the sphericity index, which is defined as $SI = (36\pi V^2)^{1/3}/S$, where SI, V, and S are the sphericity index, the entire cell volume, and the surface area, respectively[67].

The Hb concentration of the cytoplasm was obtained from the average RI value of the cytoplasm. In an aqueous solution, there stands a linear relation between the increase of RI and the concentration of the solute. The cytoplasm, which can be described as a solution of Hb, was analyzed using the following equation: $\langle \Delta n \rangle = \alpha$[Hb], where $\langle \Delta n \rangle$, α, [Hb] are the average RI increase, the RI increment, and Hb concentration, respecively[68,69]. Since the RI increment of frog Hb has not been particularly investigated, the value of α was set to 0.18 mL/g, which is the known value for human erythrocytes under illumination at 532-nm wanvelength[48,70]. Because the RI increment has a narrow range for different protein species[71] and the protein structures of Hb do not vary significantly in vertebrates[72], using the RI increment of human Hb does not mislead our study.

To investigate the deformability of individual frog erythrocytes, we analyzed the dynamic membrane fluctuations of the cells. The 2D holograms of erythrocytes were obtained with normal illumination at a frame rate of 125 Hz for two seconds. We assumed that the nuclear motion was stationary and its influence on the measured membrane fluctuations was negligible. The measured alteration of optical phase delay was interpreted into the alteration of cell thickness since the erythrocytes remained still on the coverslip during the measurements. From the measured optical phase delay image $\Delta\phi(x, y; t)$, the height fluctuation could be calculated as $h(x, y; t) = (\lambda/2\pi\langle \Delta n \rangle)\Delta\phi(x, y; t)$. We defined the dynamic membrane fluctuation σ_h as the standard deviation of the thickness profile $h(x, y; t)$ over time t.

Statistical analysis. All the numbers that follow the ±sign in the text are standard deviations. Mann-Whitney U test using an in-built MATLAB code was used for statistical comparisons between groups.

References

1. Wojtaszek, J. & Adamowicz, A. Haematology of the fire-bellied toad, Bombina bombina L. *Comparative Clinical Pathology* **12**, 129–134, https://doi.org/10.1007/s00580-003-0482-2 (2003).
2. Hota, J., Das, M. & Mahapatra, P. K. Blood Cell Profile of the Developing Tadpoles and Adults of the Ornate Frog, Microhyla ornata (Anura: Microhylidae). *International Journal of Zoology* **2013**, 14, https://doi.org/10.1155/2013/716183 (2013).
3. Wei, J. *et al*. Evolution of erythrocyte morphology in amphibians (Amphibia: Anura). *Zoologia (Curitiba)* **32**, 360–370 (2015).
4. Ruiz, G., Rosenmann, M. & Veloso, A. Respiratory and hematological adaptations to high altitude in Telmatobius frogs from the chilean andes. *Comparative Biochemistry and Physiology Part A: Physiology* **76**, 109–113, https://doi.org/10.1016/0300-9629(83)90300-6 (1983).
5. Das, M. & Mahapatra, P. K. Blood Cell Profiles of the Tadpoles of the Dubois's Tree Frog, Polypedates teraiensis Dubois, 1986 (Anura: Rhacophoridae). *The Scientific World Journal* **2012**, 11, https://doi.org/10.1100/2012/701746 (2012).

6. Fatma, D., Tosunoğlu, M. & Çiğdem, G. *Hematological values in hermaphrodite, Bufo bufo (Linnaeus, 1758)*. Vol. 5 (2009).
7. Bernard, G. W., Cooper, E. L. & Mandell, M. L. Lamellar membrane encircled viruses in the erythrocytes of Rana pipiens. *Journal of Ultrastructure Research* **26**, 8–16, https://doi.org/10.1016/S0022-5320(69)90031-8 (1969).
8. Popescu, G. *Quantitative phase imaging of cells and tissues*. (McGraw Hill Professional, 2011).
9. Lee, K. *et al*. Quantitative phase imaging techniques for the study of cell pathophysiology: from principles to applications. *Sensors* **13**, 4170–4191 (2013).
10. Kim, D. *et al*. Refractive index as an intrinsic imaging contrast for 3-D label-free live cell imaging. *bioRxiv*, 106328 (2017).
11. Popescu, G. *et al*. Imaging red blood cell dynamics by quantitative phase microscopy. *Blood Cells Mol Dis* **41**, 10–16, https://doi.org/10.1016/j.bcmd.2008.01.010 (2008).
12. Shaked, N. T., Satterwhite, L. L., Truskey, G. A., Wax, A. P. & Telen, M. J. Quantitative microscopy and nanoscopy of sickle red blood cells performed by wide field digital interferometry. *Journal of biomedical optics* **16**, 030506 (2011).
13. Park, Y. *et al*. Metabolic remodeling of the human red blood cell membrane. *Proceedings of the National Academy of Sciences* **107**, 1289 (2010).
14. Park, Y. *et al*. Measurement of red blood cell mechanics during morphological changes. *Proceedings of the National Academy of Sciences* **107**, 6731 (2010).
15. Bernhardt, I., Ivanova, L., Langehanenberg, P., Kemper, B. & von Bally, G. Application of digital holographic microscopy to investigate the sedimentation of intact red blood cells and their interaction with artificial surfaces. *Bioelectrochemistry* **73**, 92–96 (2008).
16. Choi, W. *et al*. Tomographic phase microscopy. *Nature methods* **4**, 717–719 (2007).
17. Pegard, N. C., Toth, M. L., Driscoll, M. & Fleischer, J. W. Flow-scanning optical tomography. *Lab Chip* **14**, 4447–4450, https://doi.org/10.1039/c4lc00701h (2014).
18. Kim, T. *et al*. White-light diffraction tomography of unlabelled live cells. *Nature Photonics* **8**, 256–263 (2014).
19. Cotte, Y. *et al*. Marker-free phase nanoscopy. *Nature Photonics* **7**, 113–117 (2013).
20. Kim, K. *et al*. High-resolution three-dimensional imaging of red blood cells parasitized by *Plasmodium falciparum* and *in situ* hemozoin crystals using optical diffraction tomography. *J. Biomed. Opt.* **19**, 011005–011012 (2014).
21. Habaza, M., Gilboa, B., Roichman, Y. & Shaked, N. T. Tomographic phase microscopy with 180° rotation of live cells in suspension by holographic optical tweezers. *Optics letters* **40**, 1881–1884 (2015).
22. Kim, D. *et al*. Label-free high-resolution 3-D imaging of gold nanoparticles inside live cells using optical diffraction tomography. *Methods* (2017).
23. Habaza, M. *et al*. Rapid 3D Refractive-Index Imaging of Live Cells in Suspension without Labeling Using Dielectrophoretic Cell Rotation. *Adv. Sci.* **4**, 1600205, https://doi.org/10.1002/advs.201600205 (2017).
24. Merola, F. *et al*. Tomographic flow cytometry by digital holography. *Light-Sci Appl* **6**, https://doi.org/10.1038/lsa.2016.241 (2017).
25. Villone, M. M. *et al*. Full-angle tomographic phase microscopy of flowing quasi-spherical cells. *Lab Chip* **18**, 126–131, https://doi.org/10.1039/c7lc00943g (2017).
26. Kim, G., Lee, S., Shin, S. & Park, Y. Three-dimensional label-free imaging and analysis of Pinus pollen grains using optical diffraction tomography. *Scientific Reports* **8**, 1782 (2018).
27. Wolf, E. Three-dimensional structure determination of semi-transparent objects from holographic data. *Optics Communications* **1**, 153–156 (1969).
28. Kim, K. *et al*. Optical diffraction tomography techniques for the study of cell pathophysiology. *Journal of Biomedical Photonics & Engineering* **2**, 020201 (2016).
29. Hsu, W.-C., Su, J.-W., Tseng, T.-Y. & Sung, K.-B. Tomographic diffractive microscopy of living cells based on a common-path configuration. *Optics letters* **39**, 2210–2213 (2014).
30. Hur, J., Kim, K., Lee, S., Park, H. & Park, Y. Melittin-induced alterations in morphology and deformability of human red blood cells using quantitative phase imaging techniques. *Sci Rep* **7**, 9306, https://doi.org/10.1038/s41598-017-08675-7 (2017).
31. Kim, K. *et al*. Diffraction optical tomography using a quantitative phase imaging unit. *Opt Lett* **39**, 6935–6938, https://doi.org/10.1364/OL.39.006935 (2014).
32. Park, H. *et al*. Three-dimensional refractive index tomograms and deformability of individual human red blood cells from cord blood of newborn infants and maternal blood. *J Biomed Opt* **20**, 111208, https://doi.org/10.1117/1.jbo.20.11.111208 (2015).
33. Park, H. *et al*. Measuring cell surface area and deformability of individual human red blood cells over blood storage using quantitative phase imaging. *Scientific Reports* **6** (2016).
34. Yoon, J. *et al*. Label-free characterization of white blood cells by measuring 3D refractive index maps. *Biomed Opt Express* **6**, 3865–3875 (2015).
35. Park, Y. *et al*. Refractive index maps and membrane dynamics of human red blood cells parasitized by Plasmodium falciparum. *Proc. Natl. Acad. Sci. USA* **105**, 13730–13735, https://doi.org/10.1073/pnas.0806100105 (2008).
36. Chandramohanadas, R. *et al*. Biophysics of malarial parasite exit from infected erythrocytes. *PLoS One* **6**, e20869, https://doi.org/10.1371/journal.pone.0020869 (2011).
37. Park, H. *et al*. Characterizations of individual mouse red blood cells parasitized by Babesia microti using 3-D holographic microscopy. *Scientific Reports* **5**, https://doi.org/10.1038/Srep10827 (2015).
38. Memmolo, P. *et al*. 3D morphometry of red blood cells by digital holography. *Cytometry part A* **85**, 1030–1036 (2014).
39. Shin, S. *et al*. Optical diffraction tomography using a digital micromirror device for stable measurements of 4D refractive index tomography of cells. *Proc. of SPIE*, 971814-971814-971818 (2016).
40. Kim, K. *et al*. Correlative three-dimensional fluorescence and refractive index tomography: bridging the gap between molecular specificity and quantitative bioimaging. *Biomed Opt Express* **8**, 5688–5697 (2017).
41. Shin, S., Kim, K., Yoon, J. & Park, Y. Active illumination using a digital micromirror device for quantitative phase imaging. *Optics Letters* **40**, 5407–5410 (2015).
42. Lee, K., Kim, K., Kim, G., Shin, S. & Park, Y. Time-multiplexed structured illumination using a DMD for optical diffraction tomography. *Optics Letters* **42**, 999–1002, https://doi.org/10.1364/OL.42.000999 (2017).
43. Takeda, M., Ina, H. & Kobayashi, S. Fourier-transform method of fringe-pattern analysis for computer-based topography and interferometry. *J. Opt. Soc. Am.* **72**, 156–160 (1982).
44. Debnath, S. K. & Park, Y. Real-time quantitative phase imaging with a spatial phase-shifting algorithm. *Optics Letters* **36**, 4677–4679 (2011).
45. Devaney, A. J. Inverse-Scattering Theory within the Rytov Approximation. *Optics Letters* **6**, 374–376, https://doi.org/10.1364/Ol.6.000374 (1981).
46. Lauer, V. New approach to optical diffraction tomography yielding a vector equation of diffraction tomography and a novel tomographic microscope. *Journal of Microscopy* **205**, 165–176 (2002).
47. Lim, J. *et al*. Comparative study of iterative reconstruction algorithms for missing cone problems in optical diffraction tomography. *Optics Express* **23**, 16933–16948, https://doi.org/10.1364/Oe.23.016933 (2015).
48. Lee, S. *et al*. Refractive index tomograms and dynamic membrane fluctuations of red blood cells from patients with diabetes mellitus. *Scientific Reports* **7** (2017).
49. Arserim, S. & Mermer, A. Hematology of the Uludağ Frog, Rana macrocnemis Boulenger, 1885 in Uludağ National Park (Bursa, Turkey). *E. U. J. Fish. Aquat. Sci.* **25**, 39–46 (2008).

50. Vershinin, V. L. & Vershinina, S. D. Comparative analysis of hemoglobin content in four species of anurans from the Ural uplands. *Dokl Biol Sci* **450**, 155–157, https://doi.org/10.1134/S0012496613030137 (2013).
51. Rappaz, B. *et al*. Spatial analysis of erythrocyte membrane fluctuations by digital holographic microscopy. *Blood Cells, Molecules, and Diseases* **42**, 228–232 (2009).
52. Turlier, H. *et al*. Equilibrium physics breakdown reveals the active nature of red blood cell flickering. *Nat Phys* **12**, 513–519, https://doi.org/10.1038/Nphys3621 (2016).
53. Betz, T., Lenz, M., Joanny, J. F. & Sykes, C. ATP-dependent mechanics of red blood cells. *Proc Natl Acad Sci USA* **106**, 15320–15325, https://doi.org/10.1073/pnas.0904614106 (2009).
54. Virtanen, I., Kurkinen, M. & Lehto, V. P. Nucleus-anchoring cytoskeleton in chicken red blood cells. *Cell Biol Int Rep* **3**, 157–162 (1979).
55. Chowdhury, S., Eldridge, W. J., Wax, A. & Izatt, J. A. Structured illumination multimodal 3D-resolved quantitative phase and fluorescence sub-diffraction microscopy. *Biomed Opt Express* **8**, 2496–2518 (2017).
56. Shin, S., Kim, D., Kim, K. & Park, Y. Super-resolution three-dimensional fluorescence and optical diffraction tomography of live cells using structured illumination generated by a digital micromirror device. *arXiv*, 1801.00854 (2018).
57. Park, Y. *et al*. Measurement of the nonlinear elasticity of red blood cell membranes. *Physical Review E* **83**, 051925 (2011).
58. Weber, R. E. *et al*. Novel mechanism for high-altitude adaptation in hemoglobin of the Andean frog Telmatobius peruvianus. *American Journal of Physiology-Regulatory, Integrative and Comparative Physiology* **283**, R1052–R1060 (2002).
59. Boutilier, R., Donohoe, P., Tattersall, G. & West, T. Hypometabolic homeostasis in overwintering aquatic amphibians. *Journal of Experimental Biology* **200**, 387–400 (1997).
60. Leto, T. *et al*. Comparison of nonerythroid alpha-spectrin genes reveals strict homology among diverse species. *Molecular and cellular biology* **8**, 1–9 (1988).
61. Lane, P. *et al*. Unique alpha-spectrin mutant in a kindred with common hereditary elliptocytosis. *Journal of Clinical Investigation* **79**, 989 (1987).
62. Schurmann, M., Scholze, J., Muller, P., Guck, J. & Chan, C. J. Cell nuclei have lower refractive index and mass density than cytoplasm. *J Biophotonics* **9**, 1068–1076, https://doi.org/10.1002/jbio.201500273 (2016).
63. Schurmann, M. *et al*. Three-dimensional correlative single-cell imaging utilizing fluorescence and refractive index tomography. *J Biophotonics*, e201700145, https://doi.org/10.1002/jbio.201700145 (2017).
64. Kim, K., Choe, K., Park, I., Kim, P. & Park, Y. Holographic intravital microscopy for 2-D and 3-D imaging intact circulating blood cells in microcapillaries of live mice. *Scientific reports* **6**, 33084 (2016).
65. Fedosov, D. A., Pan, W., Caswell, B., Gompper, G. & Karniadakis, G. E. Predicting human blood viscosity *in silico*. *Proceedings of the National Academy of Sciences* **108**, 11772–11777 (2011).
66. Gov, N., Zilman, A. & Safran, S. Cytoskeleton confinement and tension of red blood cell membranes. *Physical review letters* **90**, 228101 (2003).
67. Canham, P. & Burton, A. C. Distribution of size and shape in populations of normal human red cells. *Circulation Research* **22**, 405–422 (1968).
68. Barer, R. Determination of dry mass, thickness, solid and water concentration in living cells. *Nature* **172**, 1097–1098 (1953).
69. Barer, R. Interference microscopy and mass determination. *Nature* **169**, 366–367 (1952).
70. Park, Y., Yamauchi, T., Choi, W., Dasari, R. & Feld, M. S. Spectroscopic phase microscopy for quantifying hemoglobin concentrations in intact red blood cells. *Optics Letters* **34**, 3668–3670 (2009).
71. Zhao, H., Brown, P. H. & Schuck, P. On the distribution of protein refractive index increments. *Biophys J* **100**, 2309–2317, https://doi.org/10.1016/j.bpj.2011.03.004 (2011).
72. Coates, M. L. Hemoglobin function in the vertebrates: an evolutionary model. *J. Mol. Evol.* **6**, 285–307 (1975).

Acknowledgements

This work was supported by Research and Education (RnE) program, KAIST, BK21+ program, Tomocube, and National Research Foundation of Korea (2015R1A3A2066550, 2014M3C1A3052567, 2014K1A3A1A09063027).

Author Contributions

Y.S.L. and Y.P. conceived and designed the experimental idea. G.K., S.Y.Y., E.T.L., D.K., J.S. performed the experiments and analysed the data. M.L. and S.Y.L. analysed the data. All authors wrote the manuscript.

Additional Information

Competing Interests: Mr. M. Lee and Prof. Park has financial interests in Tomocube Inc., a company that commercializes optical diffraction tomography and quantitative phase imaging instruments and is one of the sponsors of the work.

Publisher's note: Springer Nature remains neutral with regard to jurisdictional claims in published maps and institutional affiliations.